Juha Heiskala, Ilkka Nissilä, Tuomas Neuvonen, Seppo Järvenpää, and Erkki Somersalo. 2005. Modeling anisotropic light propagation in a realistic model of the human head. Applied Optics, volume 44, number 11, pages 2049-2057.

Modeling anisotropic light propagation in a realistic model of the human head

Juha Heiskala, Ilkka Nissilä, Tuomas Neuvonen, Seppo Järvenpää, and Erkki Somersalo

A Monte Carlo model capable of describing photon migration in arbitrary three-dimensional geometry with spatially varying optical properties and tissue anisotropy is presented. We use the model to explore the effects of anisotropy for optical measurements of the human head. An anisotropic diffusion equation that corresponds to our Monte Carlo model is derived, and a comparison between the Monte Carlo model and the diffusion equation solution with finite elements is given. © 2005 Optical Society of America

OCIS codes: 170.5280, 170.6960, 290.1990.

1. Introduction

Diffuse optical tomography is a relatively new noninvasive medical imaging modality that makes use of visible or near-infrared (NIR) light in the wavelength range between 700 and 900 nm. The goal in optical tomography is to determine the absorption and scattering properties inside the tissue by use of measurements of the detected light on the boundary of the tissue. Strong scattering makes propagation of infrared light in most human tissues highly diffusive, which makes the task of reconstructing the internal optical properties a complicated one. To obtain a good reconstruction, the light propagation inside tissue should be modeled as faithfully as possible.

Reconstruction of the internal optical properties requires the use of iterative, nonlinear optimization techniques. In general, the solution of the forward problem needs to be calculated many times. Hence the model used has to be reasonably efficient as well as accurate. Finite-element (FE) and finite-difference formulations of the diffusion approximation (DA) to the radiative transfer equation (RTE) are commonly used as the forward model. However, the DA is known to be inaccurate in the presence of low-scattering regions such as the cerebrospinal fluid (csf) in the human head. In such cases, higher-order approximations to the RTE or Monte Carlo methods may be used. The Monte Carlo method is relatively easy to implement and it is commonly used as a reference in the validation of other numerical methods.

Many human tissues have properties that depend on direction as well as location. One example is the white matter of brain, where the orientation of axon bundles gives rise to directionally dependent diffusion properties for water molecules. Anisotropy of tissue has been shown by measurements to affect light propagation in the cases of chicken breast tissue,[1] human skin,[2] and dentin,[3] giving a good reason for believing that tissue anisotropy may have a significant effect on the signal in optical tomography.

In this paper we present a Monte Carlo model that solves the photon migration problem in an arbitrary voxel-based geometry and an arbitrary form of tissue anisotropy. We derive the anisotropic diffusion equation from the anisotropic RTE implemented by our Monte Carlo model, and a comparison between the anisotropic diffusion equation and the Monte Carlo method is given in a cylindrical geometry. We use our model to study the effects of anisotropy on light prop-

J. Heiskala (juha.heiskala@iki.fi) and T. Neuvonen are with the BioMag Laboratory and the HUS Helsinki Medical Imaging Center, respectively, Helsinki University Central Hospital, P.O. Box 340, FIN-00029 HUS, Finland. J. Heiskala, I. Nissilä, and T. Neuvonen are with the Helsinki Brain Research Centre, University of Helsinki, P.O. Box 13, FIN-00014, Finland. J. Nissilä, S. Järvenpää, and E. Somersalo are with the Helsinki University of Technology, Laboratory of Biomedical Engineering (P.O. Box 2200), Electromagnetics Laboratory (P.O. Box 3000), and Institute of Mathematics (P.O. Box 1100), respectively, FIN-02015 HUT, Finland. I Nissilä and T. Neuvonen are with the University of Helsinki: I Nissilä is with the Department of Psychology, Cognitive Brain Research Unit, P.O. Box 9, FIN-00014, Finland; T. Neuvonen is with the Department of Physiology, Neuroscience Unit, Institute of Biomedicine, P.O. Box 63, FIN-00014, Finland.

Received 28 July 2004; revised manuscript received 12 November 2004; accepted 15 November 2004.

0003-6935/05/112049-09$15.00/0

agation in the adult human head and in the head of an infant.

2. Methods

A. Monte Carlo

The Monte Carlo method provides a conceptually simple and flexible, yet rigorous, way of describing radiation transfer within tissue.

In our implementation the tissue is divided into volume elements (voxels), each of which may have different optical properties.[4] The optical properties of the model include absorption, anisotropic scattering, and the index of refraction. The rules of photon propagation were previously described in the literature.[5,6] We describe how the effect of anisotropic tissue structure may be included in the model.

To study light propagation in the human head, magnetic resonance imaging (MRI) is used to generate a geometrically accurate model of the head. Then T_1-weighted anatomical MRI voxel data are segmented into different tissue types, which are assigned optical properties according to literature values. Diffusion tensor imaging[7] (DTI) is used to obtain information about tissue anisotropy, and these data are used as the basis for modeling anisotropic light propagation in the head.

1. Photon Propagation

The forward solution in the Monte Carlo method is obtained by tracing paths of individual photons as they are scattered and absorbed within the tissue. The propagation is performed as follows.

The light source considered is a point source with a predefined spread in direction. The initial position is the same for each photon. The angle from the source axis is drawn from a uniform distribution from 0 to a predefined maximum angle, and the azimuthal angle is drawn from a uniform distribution from 0 to 2π. The weight of the photon is initialized as $w = 1$.

The path length L of the photon until the first scattering event is drawn from an exponential distribution. The absorption is handled by a reduction in the weight of the voxel by $\exp(-\mu_a L)$ at each scattering event, where μ_a is the absorption coefficient. The new direction of the photon after a scattering event is calculated by use of the probability distribution of the Henyey–Greenstein phase function[6] and scattering anisotropy factor g of the tissue in which the scattering occurs.

The propagation of the photon is continued as described above until the photon either escapes from the tissue or the weight w of the photon falls under a predefined threshold. In the latter case a technique called roulette is applied.[5] In this technique the photon is given one chance in m to continue propagation with weight mw; otherwise, the photon is extinguished.

As the anatomic model is voxel based, passing from one photon to the next one requires special treatment. At each scattering event, or after a predefined distance, which is usually set to be equal to the voxel grid spacing, a check is made of whether the photon has passed from one tissue type to another. If the tissue type has changed, the step is divided into portions in the old and new voxel and part of path length in the new voxel is renormalized by $\mu_s^{\text{old}}/\mu_s^{\text{new}}$. The absorption in each voxel is calculated according to μ_a and the length of path traveled in that voxel. If refractive index n is different in the old and new tissue types, the probability of internal reflection is calculated according to Fresnel's equation. A random number is drawn to determine whether the photon is reflected back or whether a refraction occurs. The direction of the photon is then changed in accordance with reflection of refraction, based on Fresnel's formulas.

2. Tissue Anisotropy

Our anisotropic model is based on the assumption that the directionality of white matter within the brain affects photon propagation. The possible mechanisms that could contribute are the direction-dependent scattering coefficient and direction-dependent probability distribution of the scattering phase function.

The anisotropic scattering phase function was studied by Heino *et al.*,[8] who studied the DA of the RTE and replaced the anisotropy factor g in the standard isotropic form of the equation used in optical tomography by a tensor describing preferential directions of scattering.

We adopt the approach with a direction-dependent scattering coefficient. This avoids problems of combining a direction-dependent anisotropy factor with the high isotropic anisotropy factor in biological tissues.

We model the anisotropic scattering probability by replacing the scattering coefficient μ_s by $\mu_{s,\text{iso}}\hat{\mathbf{s}}^{\mathbf{T}}\mathbf{M_s}\hat{\mathbf{s}}$. Here $\hat{\mathbf{s}}$ is the unit vector of the direction in which the photon is traveling, and $\mu_{s,\text{iso}}$ and $\mathbf{M_s}$ are the isotropic scattering coefficient and a 3×3 tensor describing the direction dependence of scattering, respectively.

The tensor $\mathbf{M_s}$ is symmetric and positive definite so that the anisotropic μ_s is positive and the same for photons traveling in exactly opposite directions. This is physically sensible, since although there is good reason to expect scattering to be different along or perpendicular to anisotropic structures, there is no reason to expect that scattering along such structures be different in opposite directions. A negative μ_s would obviously be unphysical. Furthermore, $\mathbf{M_s}$ is normalized such that the average value of $\hat{\mathbf{s}}^{\mathbf{T}}\mathbf{M_s}\hat{\mathbf{s}}$ on the unit sphere is one. This way the average value of μ_s integrated over all directions is the isotropic value $\mu_{s,\text{iso}}$.

We obviously could have included $\mu_{s,\text{iso}}$ in the tensor, but keeping the scalar value $\mu_{s,\text{iso}}$ and tensor $\mathbf{M_s}$ separate has the advantage that the user of our Monte Carlo code can change the distribution of tissue types and the isotropic $\mu_{s,\text{iso}}$ related to the tissue types without changing the anisotropy map and vice versa.

Because the Monte Carlo code allows the user to

provide the anisotropy data in different dimensions and with different orientations, a transformation matrix describing the rotations and translations necessary to transform between the coordinate systems must be given as well as the voxel dimensions of both data sets. The Monte Carlo code calculates the inverse rotation from the anisotropy data to anatomical data and rotates the $\mathbf{M_s}$ tensor so that it is aligned with the coordinate axes used in the anatomical data.

B. Diffusion Approximation

The use of finite-element method (FEM) and the DA of the RTE has become the standard way of modeling light propagation in tissue when a solution of the inverse problem of diffuse optical tomography is needed.[9,10] To implement a DA solution to the anisotropic photon propagation problem we have defined, we have to find the correct form for the anisotropic diffusion equation.

The DA is usually derived from the RTE by truncating the spherical harmonic expansions to order one (P_1 approximation).[11–14] This means in particular that some of the information about the possible anisotropies included in the RTE is lost, and the DA and the RTEs are not directly comparable. In particular, there are several possible anisotropy models of the tissue that lead formally to the same diffusion equation. In this paper we consider one such model that leads to an anisotropic diffusion equation, but one that is different from that considered in the aforementioned articles. The present RTE model is well adapted to Monte Carlo calculations, and the model can be built based on DTI data. The anisotropic RTE model is based on the following assumptions:

1. The scattering phase is rotation invariant, i.e., $\Theta(\mathbf{r}, \mathbf{s}, \hat{\mathbf{s}}') = h(\mathbf{r}, \mathbf{s}\cdot\hat{\mathbf{s}}')$ for some function h.
2. The scattering coefficient depends on the propagation angle as $\mu_s(\mathbf{r}, \hat{\mathbf{s}}) = \hat{\mathbf{s}}^{\mathbf{T}}\mathbf{M_s}\hat{\mathbf{s}}$, where $\mathbf{M_s}\in\mathbb{R}^3$ is the inverse of the diffusion tensor scaled by the trace.

These assumptions lead naturally to an anisotropic diffusion equation; furthermore, the FEM solutions seem to be in accordance with the corresponding Monte Carlo simulations, as we shall see in Subsection 3.A.

The starting point is the RTE

$$\left[\frac{1}{c}\frac{\partial}{\partial t} + \hat{\mathbf{s}}\cdot\nabla + \mu_a(\mathbf{r}) + \mu_s(\hat{\mathbf{s}}, \mathbf{r})\right]\phi(\mathbf{r}, \hat{\mathbf{s}}, t) = \mu_s\int_{\mathbb{S}^2}\Theta(\mathbf{r}, \hat{\mathbf{s}}, \hat{\mathbf{s}}')\phi(\mathbf{r}, \hat{\mathbf{s}}, t)\hat{\mathbf{s}}' + q(\mathbf{r}). \quad (1)$$

We start with the first-order approximation of ϕ with respect to the direction

$$\phi(\mathbf{r}, \hat{\mathbf{s}}, t) \approx \frac{1}{4\pi}[\rho(\mathbf{r}, t) + 3\mathbf{J}(\mathbf{r}, t)\cdot\hat{\mathbf{s}})],$$

where

$$\rho(\mathbf{r}, t) = \int_{\mathbb{S}^2}\phi(\mathbf{r}, \hat{\mathbf{s}}, t)\mathrm{d}\hat{\mathbf{s}}, \quad \mathbf{J}(\mathbf{r}, t)\int_{\mathbb{S}^2}\hat{\mathbf{s}}\phi(\mathbf{r}, \hat{\mathbf{s}}, t)\mathrm{d}\hat{\mathbf{s}}.$$

This approximation is substituted into Eq. (1). By denoting $g(\mathbf{r})$ as the *anisotropy factor* of the scattering phase function

$$g(\mathbf{r}) = \int_{-1}^{1} h(\mathbf{r}, t)t\mathrm{d}t,$$

we find, by a change of variables, that

$$\int_{\mathbb{S}^2}\Theta(\mathbf{r}, \hat{\mathbf{s}}, \hat{\mathbf{s}}')\hat{\mathbf{s}}'\mathrm{d}\hat{\mathbf{s}}' = g(\mathbf{r})\hat{\mathbf{s}}.$$

Furthermore, using the fact that

$$\int_{\mathbb{S}^2}\Theta(\mathbf{r}, \hat{\mathbf{s}}, \hat{\mathbf{s}}')\mathrm{d}\hat{\mathbf{s}}' = 1,$$

we obtain, after substituting and rearranging the terms, the approximate equation

$$\left(\frac{1}{c}\frac{\partial}{\partial t} + \hat{\mathbf{s}}\cdot\nabla\right)(\rho + 3\hat{\mathbf{s}}\cdot\mathbf{J}) = -\mu_a\rho - 3 \times [\mu_a + (1-g)\mu_s]\hat{\mathbf{s}}\cdot\mathbf{J} + q(\mathbf{r}). \quad (2)$$

To obtain the DA, we integrate Eq. (2) with respect to $\hat{\mathbf{s}}$ over $\mathbb{S}^2$. Evidently, the odd-order terms cancel by symmetry, and the even-order terms remain. Observing that

$$\int_{\mathbb{S}^2}\hat{\mathbf{s}}\hat{\mathbf{s}}^T\mathrm{d}\hat{\mathbf{s}} = \frac{4\pi}{3},$$

we get the equation

$$\frac{1}{c}\frac{\partial\rho}{\partial t} + \nabla\cdot\mathbf{J} = -\mu_a\rho + q_0, \quad (3)$$

where

$$q_0(\mathbf{r}) = \int_{\mathbb{S}^2}q(\mathbf{r}, \hat{\mathbf{s}})\mathrm{d}\hat{\mathbf{s}}.$$

On the other hand, multiplying Eq. (1) by $\hat{\mathbf{s}}$ and integrating over $\mathbb{S}^2$, we obtain by similar reasoning the equation

$$\frac{1}{c}\frac{\partial\mathbf{J}}{\partial t} + \frac{1}{3}\nabla\rho = -[\mu_a + (1-g)\mathbf{B}]\mathbf{J} + \mathbf{q}_1, \quad (4)$$

where

$$\mathbf{q}_1(\mathbf{r}) = \int_{\mathbb{S}^2} \hat{\mathbf{s}} q(\mathbf{r},\ \hat{\mathbf{s}}) \mathrm{d}\hat{\mathbf{s}},$$

and the matrix $\mathbf{B} = \mathbf{B}(\mathbf{r})$ is given as

$$\mathbf{B}(\mathbf{r}) = \frac{3}{4\pi} \int_{\mathbb{S}^2} \hat{\mathbf{s}} \mu_s(\mathbf{r},\ \hat{\mathbf{s}}) \hat{\mathbf{s}}^{\mathbf{T}} \mathrm{d}\hat{\mathbf{s}} = \frac{3\mu_{s,\mathrm{iso}}}{4\pi} \int_{\mathbb{S}^2} \hat{\mathbf{s}} \hat{\mathbf{s}}^{\mathbf{T}} \mathbf{M}_{\mathbf{s}}(\mathbf{r}) \hat{\mathbf{s}} \hat{\mathbf{s}}^{\mathbf{T}} \mathrm{d}\hat{\mathbf{s}}.$$

To integrate this expression, we choose the $\hat{\mathbf{s}}$-coordinate system such that the axii coincide with the eigenvectors of the matrix $\mathbf{M}_{\mathbf{s}}$ that are orthonormal. This leads to the expression

$$\frac{3\mu_{s,\mathrm{iso}}}{4\pi} \int_{\mathbb{S}^2} \hat{\mathbf{s}} \hat{\mathbf{s}}^{\mathbf{T}} \mathbf{M}_{\mathbf{s}}(\mathbf{r}) \hat{\mathbf{s}} \hat{\mathbf{s}}^{\mathbf{T}} \mathrm{d}\hat{\mathbf{s}} = \frac{3\mu_{s,\mathrm{iso}}}{4\pi} \int_{\mathbb{S}^2} \begin{bmatrix} s_x \\ s_y \\ s_z \end{bmatrix} (s_x^2 \lambda_1 + s_y^2 \lambda_2 + s_z^2 \lambda_3)[s_x \quad s_y \quad s_z] \mathrm{d}\hat{\mathbf{s}},$$

where the λ are the eigenvalues of $\mathbf{M}_{\mathbf{s}}$.

We do the above integration in spherical coordinates. The components of the unit vector $\hat{\mathbf{s}}$ are written

$$s_x = \sin\theta \cos\phi, \qquad s_y = \sin\theta \sin\phi, \qquad s_z = \cos\theta,$$

and the integration yields

$$\begin{aligned} &\frac{3\mu_{s,\mathrm{iso}}}{4\pi} \int_{\phi=0}^{2\pi} \int_{\theta=0}^{\pi} \hat{\mathbf{s}}(\theta,\ \phi)(1-g) \hat{\mathbf{s}}^{\mathbf{T}}(\theta,\ \phi) \mathbf{M}_{\mathbf{s}} \hat{\mathbf{s}}(\theta,\ \phi) \\ &\quad \times \hat{\mathbf{s}}^{\mathbf{T}}(\theta,\ \phi) \sin(\theta) \mathrm{d}\theta \mathrm{d}\phi \\ &= \frac{\mu_{s,\mathrm{iso}}}{5} (1-g) \\ &\quad \times \begin{bmatrix} 3\lambda_1 + \lambda_2 + \lambda_3 & 0 & 0 \\ 0 & 3\lambda_2 + \lambda_1 + \lambda_3 & 0 \\ 0 & 0 & 3\lambda_3 + \lambda_1 + \lambda_2 \end{bmatrix}. \end{aligned} \tag{5}$$

Thus we obtain an anisotropic diffusion equation in which the isotropic scattering coefficient μ_s is replaced by a tensor

$$\mathbf{T}_{\mu_s} = \frac{\mu_{s,\mathrm{iso}}}{5} \times \begin{bmatrix} 3\lambda_1 + \lambda_2 + \lambda_3 & 0 & 0 \\ 0 & 3\lambda_2 + \lambda_1 + \lambda_3 & 0 \\ 0 & 0 & 3\lambda_3 + \lambda_1 + \lambda_2 \end{bmatrix}. \tag{6}$$

Instead of the diffusion coefficient D in the isotropic case, we now get a diffusion tensor

$$\mathbf{D} = (1/3)[\mu_a \mathbf{I} + (1-g)\mathbf{T}_{\mu_s}]^{-1}, \tag{7}$$

where $\mathbf{I}$ is the unit matrix and $\mathbf{T}_{\mu_s}$ is the tensor describing the directionally dependent scattering coefficient as given in Eq. (6).

We show the calculation for the case in which the anisotropy axes are parallel to the Cartesian coordinate axes, but the diffusion tensor for anisotropy with different anisotropy axes is obtained easily by rotating the tensor $\mathbf{D}' = \mathbf{R}\mathbf{D}\mathbf{R}^{\mathbf{T}}$, where $\mathbf{R}$ is the rotation matrix.

The diffusion equation derived above can be solved by use of FEM. This requires altering the standard implementation to accommodate a diffusion tensor instead of a diffusion coefficient.

C. Anatomic Tissue Model

We study the effect of anisotropy on light propagation in the human head. The anatomic model used includes a map of the spatial distribution of different tissue types within the head and a map of the spatial distribution of anisotropy. We want to study the effect of tissue anisotropy caused by white matter tracts within the brain, and therefore anisotropic effects are restricted to white matter in the model.

1. Anatomic Magnetic Resonance Data

Anatomic data were obtained with the Siemens Magnetom Sonata 1.5T scanner. A high-resolution three-dimensional T_1-weighted scan was performed that produced a three-dimensional data set with cubic 1-mm^3 voxels and dimensions 256 mm $\times$ 256 mm $\times$ 180 mm.

The T_1-weighted image was segmented into seven tissue types, including the scalp, skull, white and gray brain matter, and csf. In addition, regions within the csf containing an especially large amount of trabecular membranes, as well as the superior sagittal sinus (a large vein that runs close to skull between the left and the right lobes of the brain), were treated as separate tissue types. The segmentation was performed semiautomatically, using software provided by Neuromag.[15] Figure 1 illustrates the segmentation result.

The optical properties of the tissue types were taken partly from the literature, and the scalp and the skull scattering and absorption coefficients were determined by performing a fit between the Monte Carlo simulation results and the measurements taken by the 16-channel frequency-domain optical measurement device developed at the Laboratory of Biomedical Engineering of the Helsinki University of Technology.[16] The optical properties for the tissue types are given in Table 1.[17–19]

2. Diffusion Tensor Magnetic Resonance Data

We used diffusion tensor magnetic resonance (MR) data to obtain information on the anisotropic structure of the brain. DTI measures the diffusion of water

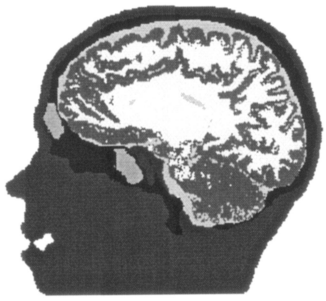

Fig. 1. Sagittal slice of the segmented MRI data. In the slice are shown the segmented scalp, skull, and brain. Nonsegmented tissues are put together with scalp, and they do not contribute much to the signal in typical imaging setups. Also shown in the slice are two sinuses (empty spaces inside the bone of the skull).

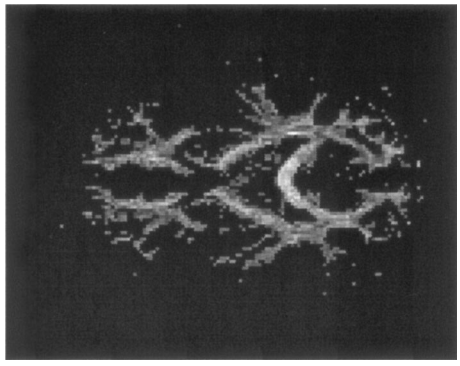

Fig. 2. Transaxial slice of a three-dimensional fractional anisotropy index map calculated from our DTI data. To make the image clearer, we show only fractional anisotropy values above 0.3.

molecules and its directional dependence, and it is capable of identifying large white matter tracts within the brain. Our assumption in constructing the model was that NIR light propagation is affected by these white matter tracts as well and that the direction dependence of the diffusion of photons is roughly similar to the direction dependence of the diffusion of water molecules.

This assumption seems reasonable considering that light propagation along and perpendicular to muscle fibers in chicken breast tissue have been measured[1] to differ. White matter tracts, like muscles, contain tubular structures that allow easy diffusion of water and solvents in the direction of the tubes and weaker diffusion in the perpendicular direction.

DTI was performed with the same device that was used for the anatomic scan. Diffusion-weighted data were acquired with an echo-planar imaging sequence, using 36 4.0-mm-thick axial slices with 128 $\times$ 128 voxels with x and y dimensions of 1.75 mm $\times$ 1.75 mm. The diffusion-weighting gradients were applied in 12 noncollinear directions, and the diffusion tensors $\mathbf{D_{MR}}$ were estimated for each voxel by use of a least-squares approach.[20]

A convenient measure of the direction dependence of water diffusion that can be calculated from DTI data is the fractional anisotropy index.[21] It is a measure that is zero when diffusion is isotropic and close to one when one diffusion direction is dominant. Figure 2 shows a map of fractional anisotropy index calculated from our DTI data. White matter tracts can be seen in the image, demonstrating their importance as a source of tissue anisotropy.

Using the diffusion tensor $\mathbf{D_{MR}}$ obtained from the DTI scan, we may express the diffusion coefficient for water molecules for any direction as

$$\hat{\mathbf{v}}^{\mathbf{T}}\mathbf{D_{MR}}\hat{\mathbf{v}}, \tag{8}$$

where $\hat{\mathbf{v}}$ is a unit vector in the desired direction. This expression is of the same form as the relation $\mu_{s,\mathrm{iso}}\hat{\mathbf{s}}^{\mathbf{T}}\mathbf{M_s}\hat{\mathbf{s}}$ that we use to calculate the direction-dependent scattering coefficient in a particular direction. The difference is that in the case of water diffusion, a large diffusion coefficient in a particular direction implies that water molecules tend to move preferentially along that direction, whereas in our case, a large scattering coefficient in a particular direction tends to deflect photons from that direction and results in weaker diffusion.

In most tissues, including white matter, scattering dominates over absorption of photons, and in such cases the diffusion equation represents a fairly good approximation of photon propagation. In the standard diffusion equation, when $\mu_s \gg \mu_a$, the diffusion coefficient is approximately inversely proportional to the scattering coefficient. We use this approximate inverse proportionality to calculate the scattering coefficient tensor $\mathbf{M_s}$ from the diffusion tensor $\mathbf{D_{MR}}$ for water as

$$\mathbf{M_s} = \frac{\mathbf{E}^{\mathbf{T}}\mathbf{\Lambda}^{-1}\mathbf{E}}{(1/3)\mathrm{trace}(\mathbf{\Lambda}^{-1})}, \tag{9}$$

where $\mathbf{E}$ is a 3×3 matrix holding the eigenvectors of $\mathbf{D_{MR}}$ as its columns and $\mathbf{\Lambda}$ is a diagonal matrix with the corresponding eigenvalues as its diagonal elements. The normalization by $(1/3)\mathrm{trace}(\mathbf{\Lambda}^{-1})$ is chosen so that the average value of $\hat{\mathbf{s}}^{\mathbf{T}}\mathbf{M_s}\hat{\mathbf{s}}$ integrated over the unit sphere is 1, giving an average scattering coefficient $\mu_{s,\mathrm{iso}}$.

Since the field of view and orientation of slices in the T_1 and DT images were different, and the possi-

Table 1. Optical Properties of Tissue Types

Tissue Type	$\mu_s(\mathrm{mm}^{-1})^a$	g	$\mu_a(\mathrm{mm}^{-1})$	n
Scalp	10	0.9	0.018	1.3
Skull	13	0.9	0.016	1.3
Gray matter	44	0.95	0.036	1.3
White matter	91	0.9	0.014	1.3
Cerebrospinal fluid	0.001	0.9	0.002	1.3
Trab. membranes[b]	16	0.95	0.016	1.3
Sup. sag. sinus[c]	20	0.95	0.3	1.3

[a]Note that μ_s instead of $\mu_s' = (1 - g)\mu_s$ is given.
[b]Trab. membranes, trabecular membranes.
[c]Sup. sag. sinus, superior sagittal sinus.

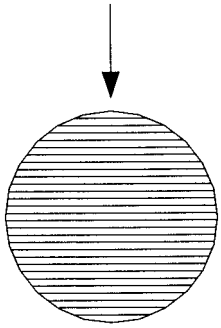

Fig. 3. Schematic drawing of the setup for the calculation of the effect of anisotropy in a cylinder.

bility that the subject moved between the measurements had to be taken into account, coregistering the images to each other was necessary. We used a linear registration tool called FLIRT[22] (FMRIB's Linear Image Registration Tool) to do this. We calculated an affine transformation from anatomic to DT coordinates and the rotation part of the inverse transformation. The latter was used for rotating the diffusion tensors to align them to the coordinate axis of the anatomic data.

The registration maps corresponding voxels in both data sets onto each other with good accuracy in most of the brain. However, because of echo-planar imaging distortion[23] in the frontal region of the brain, voxels in this region are not necessarily correctly mapped.

3. Results

A. Monte Carlo and Diffusion Equation Solutions

In Subsection 2.B we showed how the anisotropy model we defined in the RTE can be implemented in DA.

We used our three-dimensional FEM code to solve the diffusion equation in a simple cylindrical geometry. The same calculations were also performed with our anisotropic Monte Carlo code. In the calculation, 1 source and 31 detectors were placed in a plane along the circumference of a cylinder at equal distances from one another. The radius of the cylinder was 20 mm and the height 60 mm. The source was modulated at a 100-Mhz frequency. The optical properties of the cylinder were $\mu_s = 1.0\ \mathrm{mm}^{-1}$, $g = 0$, $\mu_a = 0.01\ \mathrm{mm}^{-1}$, $n = 1.4$. Solutions were calculated for an isotropic case and for an anisotropic case with uniform anisotropy in the direction perpendicular to the direction of the source and to the axis of the cylinder. The situation is illustrated in Fig. 3.

The $\mathbf{T}_{\mu_s}$ tensor used in the Monte Carlo calculation was chosen to be $\mathbf{T}_{\mu_s} = \mathrm{diag}(1.4615, 0.0769, 1.4615)$. Using Eq. (7), we get $\mathbf{D} = \mathrm{diag}(0.2797, 0.9332, 0.2797)$ for the diffusion tensor in the FEM calculation.

In Figs. 4 and 5, the phase shift and logarithm of the photon flux amplitude are shown for the isotropic and anisotropic cases. In the Monte Carlo simulation,

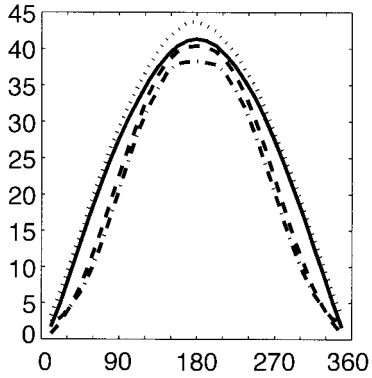

Fig. 4. Phase shift in the case of a cylindrical geometry. On the y axis, the phase shift in degrees is shown, and the x coordinate is the angle in degrees between the source and the detector along the cylinder circumference. The isotropic case calculate with FEM and Monte Carlo are given by the solid and dotted curves, respectively. The anisotropic case calculated with FEM and Monte Carlo are given by the dashed and dashed–dotted curves, respectively.

1.6×10^8 photon paths were traced, and in the FEM calculation, a mesh with approximately 1.5×10^5 quadratic volume elements was used. Both the number of photons traced and the refinement of the mesh were tested to be sufficient for convergence of the numerical results.

The results of this comparison show that there are differences between the RTE (Monte Carlo) and diffusion equation solutions, but qualitatively the results of the two methods agree. In both the FEM and the Monte Carlo calculation, the addition of anisotropy produces very similar results.

B. Effects of Anisotropy in a Realistic Head Model

We used our Monte Carlo model to carry out a simulation of the effects of tissue anisotropy in a realistic situation involving a single source position and several detectors on the same side of the head.

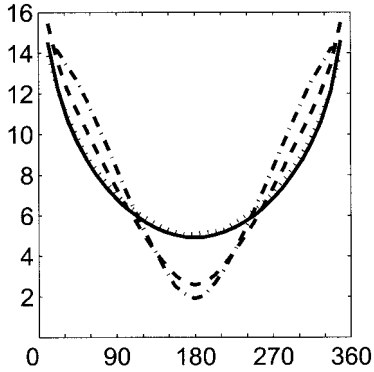

Fig. 5. Logarithm of amplitude in the case of a cylindrical geometry. On the y axis is shown the logarithm of amplitude (arbitrary units), and the x coordinate is the angle in degrees between the source and the detector along the cylinder circumference. The isotropic case calculate with FEM and Monte Carlo are shown by the solid and dotted curves, respectively. The anisotropic case calculated with FEM and Monte Carlo are given by the dashed and dashed–dotted curves, respectively.

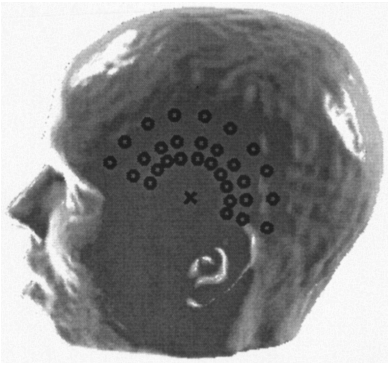

Fig. 6. View of the array of source and detector fibers used in our head imaging simulation. The source is shown as a black "x" and the detectors as black circles. The detectors are divided into 3 groups of 10 detectors at a fixed distance from the source. In each group, detectors are mapped from the back toward the front of the head, or counterclockwise in the figure.

We calculated the signal recorded at the detectors in the case of a frequency-domain measurement with modulation frequency $f = 100$ MHz when tissue anisotropy is taken into account, and when it is not taken into account.

Our anatomic model is based on MR imaging of an adult subject. However, we also wanted to study the effect of anisotropy in optical imaging of an infant. We were motivated by the fact that owing to the smaller size of the head of an infant, deeper tissues can be imaged. Therefore the anisotropy present in the white matter can be expected to have more of an effect when imaging the head of an infant.

Since DT images of an infant were not available to us, we approximated the head of a newborn infant by scaling our adult tissue model by a factor of 0.5. Although this is obviously inaccurate, it allows us to obtain an approximation of the effect that anisotropy may have in the case of an infant.

In both adult and infant cases, the light source was simulated by injecting photons into the tissue model at the left side of the head, slightly up and toward the nose from the highest point of the earlobe. Exiting photons were counted at 30 detector locations on the surface of the tissue model. These were divided into 3 groups of 10, with each group lying on an approximate semicircle with the center of the circle at the light source. In each group the detectors were numbered 1 to 10 from the rear toward the front of the head. The radii of the semicircles were different in the two cases we studied, and they are given separately for each case. The arrangement of the detector locations is illustrated in Fig. 6. The detector locations in the simulations were chosen such that a similar detector array might be used in actual imaging of the auditory brain cortex.

Estimates for the statistical inaccuracy of the Monte Carlo simulation for the amplitude and the phase shift were obtained by dividing the Monte Carlo photon runs into subsamples. The standard deviation between the subsamples provided an estimate for the error in the amplitude and phase shift obtained from the simulation. The statistical significance of the anisotropic effect was tested using the paired t-test.

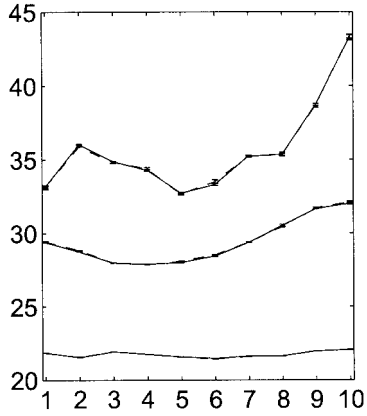

Fig. 7. Phase shift in the simulated measurement of an adult head. The y axis shows the magnitude of the phase shift in degrees, and the x axis shows the detector number. Solid and dashed curves represent the results of the isotropic and anisotropic cases, respectively. In each semicircular group of detectors, the detectors are numbered counterclockwise from 1 to 10. The phase shift increases with increasing distance from the source.

1. Adult Head

In the case of the adult head, the three groups of detectors were at distances of approximately 25, 35, and 50 mm. The source was placed 10 mm above and 20 mm toward the nose from the highest point of the earlobe.

The simulated phase shift and logarithm of amplitude in the detectors are shown in Figs. 7 and 8, respectively. In both figures, isotropic and anisotropic cases are presented by different curves. Especially in the case of logarithm of amplitude, however, the difference between the curves is so small that they ap-

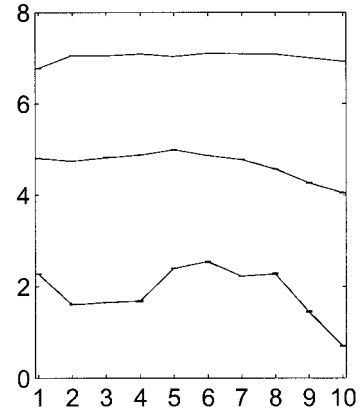

Fig. 8. Logarithm of amplitude in the simulated measurement of an adult head. The y axis shows the logarithm of amplitude (arbitrary units), and the x axis shows the detector number. The isotropic and anisotropic cases are given by the solid and dashed curves, respectively. In each semicircular group of detectors, the detectors are numbered counterclockwise from 1 to 10. The amplitude decreases with increasing distance from the source.

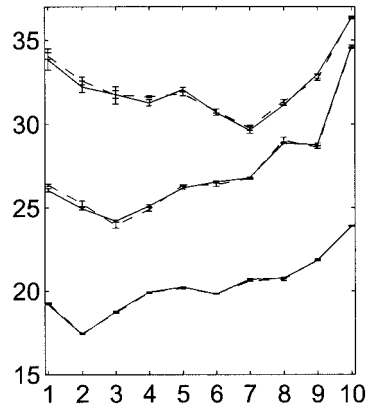

Fig. 9. Phase shift of the signal in the simulated measurement of an infant head. The y axis shows the phase shift in degrees, and the x axis shows the detector number. Solid and dashed curves represent the results of the isotropic and anisotropic cases, respectively. In each semicircular group of detectors, the detectors are numbered counterclockwise from 1 to 10. The phase shift increases with increasing distance from the source.

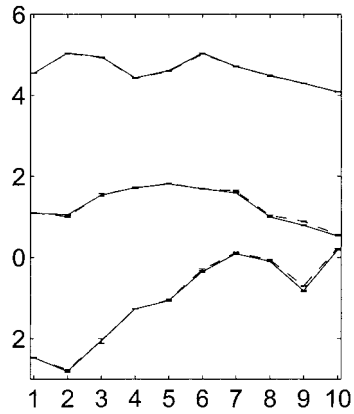

Fig. 10. Logarithm of amplitude in the simulated measurement of an infant head. The y axis shows the logarithm of amplitude (arbitrary units), and the x axis shows the detector number. Solid and dotted curves represent the results of the isotropic and anisotropic cases, respectively. In each semicircular group of detectors, the detectors are numbered counterclockwise from 1 to 10. The amplitude decreases with increasing distance from the source.

pear as one curve. Error estimates for each case are given by the error bars on the curves.

For the adult case, we see no statistically significant anisotropy effect for amplitude or phase shift in any of the detectors. The largest difference in amplitude between the isotropic and the anisotropic cases is of the order of 1.5%, and the largest difference in phase shift is approximately 0.6 deg. These differences are within the statistical error of the simulation.

2. Infant Head

For the infant head, the source–detector distances for the three groups were approximately 30, 40, and 50 mm. The exact distance varied because of the shape of the head. The source was placed 5 mm above and 10 mm toward the nose from the highest point of the earlobe.

The simulated phase shift and logarithm of amplitude in the detectors for the infant head are shown in Figs. 9 and 10. The isotropic and anisotropic cases are presented by different curves. The error estimates for each case are given by the error bars on the curves.

For amplitude, clear and statistically significant differences in the results of the isotropic and anisotropic simulations are seen in detectors 7 and 9 of the outermost detector group and in detector 9 of the middle detector group (p-values ≤ 0.025). The greatest difference in the amplitude is found in detector 9 of the outermost group, where it corresponds to a 12% difference between the isotropic and the anisotropic cases. For detector 9 of the middle detector group, we see a 10% signal change between the isotropic and the anisotropic cases.

For the phase shift, we see a statistically significant anisotropy effect in the same detectors as for the amplitude (p-values ≤ 0.03). However, the effect is quite small (of the order of 0.5 deg).

We note that in the case of the infant head, our model already predicts a measurable change in the amplitude at a distance of 40 mm between the source and the detector. In reality, even a shorter distance may be sufficient because the scalp and skull of an actual infant are thinner than in our scaled-down model of an adult head. Also, the optical properties used for the brain tissue in this study were those of an adult. The differences between these and the optical properties of the brain tissue of an infant may cause further differences in the significance of anisotropy in the imaging of adults versus infants.

4. Discussion

In this paper we have presented a model for tissue anisotropy in optical imaging. We have described a Monte Carlo model that is capable of performing simulations based on this anisotropy model in arbitrary geometry and in arbitrarily shaped anisotropy, and we have derived the form of the DA of the RTE by using the anisotropy model we have chosen.

The simulations we have performed in a realistically shaped head model suggest that in the case of the adult human head, the effect of tissue anisotropy on the measured optical signal is very small. In the case of an infant head, our simulated data shows a significant phase and amplitude effect that is due to anisotropy in the reflection geometry. In optical tomography of premature infants, transmission measurements are used, and in such a case we expect to see a much more pronounced effect owing to anisotropic light propagation in the white matter. This is the topic of further study.

The authors would like to thank the Finnish Cultural Foundation, The Finnish Academy of Science and Letters, The Finnish Foundation for the Advancement of Technology, the Jenny and Antti Wihuri Foundation, and the Instrumentarium Science Foundation for support. The use of the computing facilities of the Finnish IT center for science

(CSC) is gratefully acknowledged. J. Heiskala and T. Neuvonen wish to acknowledge funding from special governmental grants for health sciences research TYH 4212 and TYH 4249, respectively.

References

1. G. Marquez, L.-H. Wang, S.-P. Lin, J. A. Schwartz, and S. L. Thomsen, "Anisotropy in the absorption and scattering spectra of chicken breast tissue," Appl. Opt. **37,** 798–804 (1998).
2. S. Nickell, M. Hermann, M. Essenpreis, T. J. Farrell, U. Krämer and M. S. Patterson, "Anisotropy of light propagation in human skin," Phys. Med. Biol. **45,** 2873–2886 (2000).
3. A. Kienle, F. K. Forster, R. Diebolder, and H. Hibst, "Light propagation in dentin: influence of light propagation on anisotropy," Phys. Med. Biol. **48,** N7–N14 (2003).
4. D. A. Boas, J. P. Culver, J. J. Stott, and A. K. Dunn, "Three-dimensional Monte Carlo code for photon migration through complex heterogenous media including the adult human head," Opt. Express **10,** 159–170 (2002), http://www.opticsexpress.org.
5. S. A. Prahl, M. Keijzer, S. L. Jacques, and A. J. Welch, "A Monte Carlo model of light propagation in tissue," in *Dosimetry of Laser Radiation in Medicine and Biology*, G. J. Müller and D. H. Sliney, eds., Proc. SPIE **5,** 102–111 (1989).
6. L. Wang, S. L. Jacques, and L. Zheng, "MCML-Monte Carlo modeling of light transport in multi-layered tissues," Comput. Methods Programs Biomed. **47,** 131–146 (1995).
7. P. J. Basser, J. Mattiello, and D. Le Bihan, "MR diffusion tensor spectroscopy and imaging," Biophys. J. **66,** 259–267 (1994).
8. J. Heino, S. Arridge, J. Sikora, and E. Somersalo, "Anisotropic effects in highly scattering media," Phys. Rev. E **68,** 31908 (2003).
9. M. Schweiger, S. R. Arridge, M. Hiraoka, and D. T. Delpy, "Application of the finite element method for the forward model in infrared absorption imaging," in *Mathematical Methods in Medical Imaging*, D. C. Wilson and J. N. Wilson, eds., Proc. SPIE **1768,** 97–108 (1992).
10. M. Schweiger, S. R. Arridge, M. Hiraoka, M. Firbank, and D. T. Delpy, "Comparison of a finite-element forward model with experimental phantom results: application to image reconstruction," in *Photon Migration and Imaging in Random Media and Tissues*, B. Chance and R. R. Alfano, eds., Proc. SPIE **1888,** 179–190 (1993).
11. S. Arridge, "Optical tomography in medical imaging," Inverse Probl. **15,** R41–R93 (1999).
12. J. Heino and E. Somersalo, "Estimation of optical absorption in anisotropic background," Inverse Probl. **18,** 559–573 (2002).
13. N. Hyvönen, "Analysis of optical tomography with non-scattering regions," Proc. Edinburgh Math. Soc. **45,** 257–276 (2002).
14. J. Kaipio and E. Somersalo, *Statistical and Computational Inverse Problems* (Springer-Verlag, Berlin, 2004).
15. Seglab software, Elekta Neuromag Oy, P.O. Box 68, FIN-00511 Helsinki, Finland (Elimäenkatu 22, FIN-00510 Helsinki).
16. I. Nissilä, T. Naponen, K. Kotilahti, T. Tarvainen, M. Schweiger, L. Lipiäinen, S. Arridge, and T. Katila, "Instrumentation and calibration methods for the multichannel measurement of phase and amplitude in optical tomography," Rev. Sci. Instrum. (to be published).
17. E. Okada and D. T. Delpy, "Near-infrared light propagation in an adult head model. I. Modeling of low-level scattering in the cerebrospinal fluid layer," Appl. Opt. **42,** 2906–2914 (2003).
18. C. R. Simpson, M. Kohl, M. Essenpreis, and M. Cope, "Near-infrared optical properties of *ex vivo* human skin and subcutaneous tissue measured using the Monte Carlo inversion technique," Phys. Med. Biol. **43,** 2465–2478 (1998).
19. M. Firbank, M. Hiraoka, M. Essenpreis, and D. T. Delpy, "Measurement of the optical properties of the skull in the wavelength range 650–950 nm," Phys. Med. Biol. **38,** 503–510 (1993).
20. N. G. Papadakis, D. Xing, C. L. H. Huang, L. D. Hall, and T. A. Carpenter, "A comparative study of acquisition schemes for diffusion tensor imaging using MRI," J. Magn. Reson. B **137,** 67–82 (1999).
21. P. J. Basser and C. Pierpaoli, "Microstructural and physiological features of tissues elucidated by quantitative-diffusion-tensor MRI," J. Magn. Reson. B **111,** 209–219 (1996).
22. M. Jenkinson and S. Smith, "A global optimisation method for robust affine registration of brain images," Med. Image Anal. **5,** 143–156 (2001).
23. P. Jezzard and R. S. Balaban, "Correction for geometric distortion in echo planar images from B_0 field variation," Magn. Reson. Med. **34,** 65–73 (1995).